Applied Physics Express 11, xxxxxx (2018)
https://doi.org/10.7567/APEX.11.xxxxxx

APEX PROOF

Superlens-enhanced laser interference lithography

Xudong Guo[1], Li Li[1]*, Yaowei Hu[1], Liang Cao[1], Litong Dong[1], Lu Wang[1]*, Ran Ding[1], Zhankun Weng[1], Zhengxun Song[1], Hongmei Xu[1], Zhen Yang[2], Xianping Liu[2], Yanling Tian[2], and Zuobin Wang[1]*

[1]*International Research Centre for Nano Handling and Manufacturing of China (CNM), Changchun University of Science and Technology, Changchun 130022, China*
[2]*School of Engineering, University of Warwick, Coventry CV4 7AL, U.K.*
*E-mail: lil@cust.edu.cn; wangl@cust.edu.cn; wangz@cust.edu.cn

Received September 20, 2018; accepted October 22, 2018; published online xxxx yy, zzzz

A one-step lithography method based on a superlens is proposed to fabricate diffraction-unlimited metallic patterns. By controlling the material parameters and the distribution of the impinging energy, various phenomena, such as periodic nanonetworks, ultrathin nanowires (sub-50-nm feature size), and variable-sized nanoparticles (ranging from sub-10 nm to several hundreds of nanometers), are fabricated using a 1,064-nm nanosecond laser. The evolution pathway of such phenomena is explained by the dewetting process of metallic films. The direct-writing performance of a transparent material with a superlens is studied, and the maximum etching depth of Si gratings can reach 2 μm under a single laser pulse, with fine profiles. © 2018 The Japan Society of Applied Physics

Recently, with achievements in nanotechnology and the demands for practical applications of nanotechnology in daily life, there has been increasing demand for next-generation ultrahigh-resolution (even sub-10 nm)[1] lithography technologies that are low-cost and high-throughput and can be applied to a wide range of material systems. At present, the relatively mature and ultrahigh-resolution lithography techniques include electron-beam lithography (EBL),[2] focused ion-beam lithography (FIBL),[3] scanning probe lithography (SPL),[4] laser scanning lithography (LSL),[5] nanoimprint lithography (NIL),[6] and nanosphere lithography.[7] However, EBL, FIBL, and LSL, which have feature sizes of <30 nm, are not suitable for mass production, owing to their problems related to time consumption. NIL enjoys the advantages of a high resolution and arbitrary pattern. However, the fabrication of a template is limited to planar technology, which requires a complex and expensive process. The microelectronics industry, which uses deep ultraviolet/extreme ultraviolet lithography and other methods, achieves resolutions as high as sub-10 nm but at very high costs. On one hand, the microelectronics industry is researching methods for reducing costs. On the other hand, in many relatively low value-added fields, such as quantum dots, grating rulers, energy, and metasurface optics, low-cost lithography is required for large-scale and rapid manufacturing for businesses to remain competitive. Another problem is that the aforementioned lithography methods always need to be combined with subsequent etching processes for deep structures, such as reactive-ion etching[8] and metal-catalyzed electroless etching,[9] which require complex equipment or toxic reagents.

Laser interference lithography (LIL) is a large-scale, rapid, and direct-writing lithography technique that can be applied at the microscale and nanoscale.[10] The sophisticated energy distribution of a light field in a three-dimensional (3D) space can be generated by altering the numbers of coherent laser beams, the azimuthal angles, the polarization states, and other parameters.[11] LIL is widely used in the processing of two-dimensional and 3D pattern structures in areas such as grating rulers,[12] solar cells,[13] photonic crystals,[14] lithium batteries,[15] and optical devices[16] and thus has received extensive attention. However, achieving a high resolution similar to that of EBL, FIBL, SPL, LSL, and other technologies is relatively difficult for LIL and often requires increasing the complexity of the equipment and technology.[17] Additionally, LIL has a poor capability to process transparent materials and cannot satisfy demands for transparent metamaterials and transparent optical materials with hydrophobic, antifogging, and antireflective properties.

In this study, metallic superlenses are introduced into LIL, yielding a technique that we denote as superlens-enhanced LIL (SELIL). A thin metallic slab coated on the Si substrate functions as a superlens that generates surface plasma polaritons (SPPs), concentrating the evanescent subwavelength field and allowing a super resolution.[18] Our simulations showed that the sub-wavelength information is enhanced near the interface owing to the existence of the superlens, resulting in a large energy change within a narrow linewidth. Because of the high threshold and nonlinear absorption of metallic films, the sub-wavelength information is recorded during the dewetting process of metallic films. After re-solidification within several nanoseconds, sub-100-nm Pt nanopatterns, including nanonetworks, nanoparticles, and nanowires, are formed.

In the experiments, Si substrates were cleaned in an orderly manner under the action of acetone, ethanol, and deionized water via an ultrasonic process. Each type of solution was used three times, and a single ultrasonic process took 5 min. P-type single-polished Si(100) wafers with a resistivity of approximately 10 Ω·cm were used in the experiments. Metal layers, including Pt, Au, Ag, Al, and Ni, with various thicknesses were deposited on the Si surfaces using an ion-sputtered coater (Quorum Technologies Q150T). The thickness was controlled by a film-thickness monitor. Interference patterns were created on the samples by building and applying a low-cost, lens-free, and direct LIL system [Fig. 1(a), left] with a single pulse, where the coherent source was a Nd:YAG nanosecond laser (Innolas) with a wavelength of 1,064 nm, a Gaussian beam diameter of 6 mm, and 7-ns pulses. The three divided beams of the LIL system had the same incident angles (to obtain different periods of the pattern, the angles were altered between 3.4 and 7.6°), and the azimuthal angles were 0, 120, and 240°. The polarizer angles were 0, 90, and 90°. A flap was used to control the number of incident beams. The energy of a single laser beam was varied from 30 to 160 mJ, which was detected by a photometer. The power was controlled by altering the voltage of the laser source. The voltage applied in our experiments varied from 500 to 620 V. Scanning electron microscopy (Thermo Fisher Helios G4) was performed to study the interference pattern after the exposure. All experiments were conducted in a clean environment.

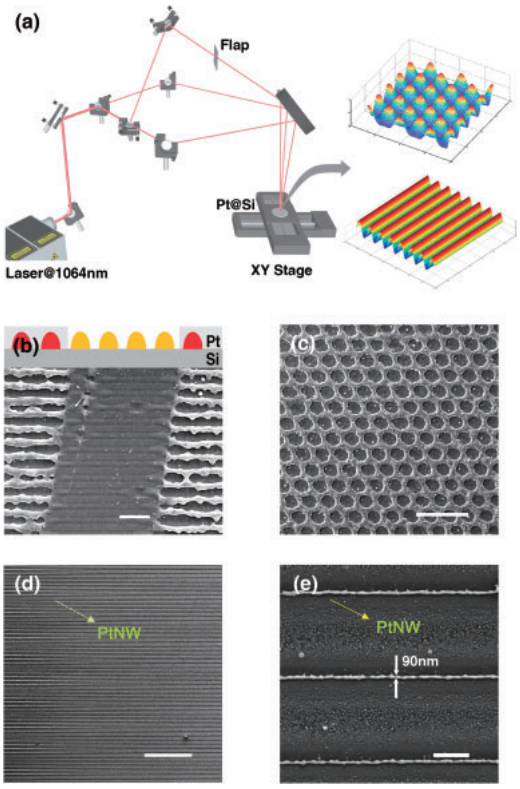

Fig. 1. (a) (Left) Setup of a direct LIL system and (right) simulation results of the 3D intensity distributions[25] of two- and three-beam LIL patterns. Exposed deep Si structures with a single laser pulse under (b) two-beam and (c) three-beam LIL when coated with a Pt superlens slab. The red color represents a higher intensity resulting from the superlens, and the yellow color represents a lower intensity without the superlens. The scale bars represent 20 μm. Fabricated PtNWs in (d) a large area and (e) with a super resolution. The scale bars represent 100 and 2 μm, respectively.

Because of the low optical absorbance of Si at 1,064 nm (0.067%),[19] direct writing and patterning of Si is difficult. Thus, the direct-writing performance is usually enhanced by adopting corrosive gases[20] or applying high-power and multi-pulse laser irradiation,[21] as in our previous work.[22] Herein, a superlens is proposed to write deep Si structures. In the experiment, an 80-nm-thick Pt superlens was applied, and the results are shown in Fig. 1. However, the exposed Si gratings without a superlens are not as obvious as the central line shown in Fig. 1(b), where the superlens was removed using a tweezer tip. In this area, the bumps are not concave, as they are formed on the lines with the maximum intensity distribution resulting from the Marangoni effect.[23] In contrast, the deep concave at the edge in Fig. 1(b) is caused by explosive boiling[24] of the bumps with the aid of the superlens. The structure shown in Fig. 1(c) is a moth-eye structure[25] with outstanding anti-reflective properties. The information of the profile is shown in Figs. S1.1 and S1.2 in the online supplementary data at http://stacks.iop.org/APEX/11/000000/mmedia. Thus, SELIL is a promising one-step method for obtaining a large-scale anti-reflective surface compared with the conventional complex method of fabricating a moth-eye structure, i.e., reactive-ion etching.[26] In addition to the substrate, the Pt superlens can be directly written to obtain diffraction-unlimited metallic nanopatterns. Figure 1(d) shows the Pt nanowires (PtNWs) fabricated over a large area. The feature size of the PtNWs in Fig. 1(e) is 90 nm, which is beyond the Rayleigh–Abbe diffraction limit.[18] Further detailed information is presented in Sect. 2 of the online supplementary data at http://stacks.iop.org/APEX/11/000000/mmedia. The relationship between the exposed Si patterns and the PtNWs is shown in Fig. 3. Other sub-100-nm Pt patterns are shown in the online supplementary data at http://stacks.iop.org/APEX/11/000000/mmedia. For example, nanowires and nanoparticles are shown in Figs. S3 and S4.

The physical mechanisms underlying the fabricated diffraction-unlimited nanopatterns are mainly attributed to three aspects. First, the SPPs generated at the interface between the superlens and the Si slab enhance the evanescent waves, which not only increases the near-field energy but also determines the smallest feature size of the nanopattern. Second, periodic and variable-sized nanopatterns are induced by the complicated interference field distribution. Third, the concept of pulsed laser dewetting is introduced to explain the evolution of different nanopatterns caused by the laser intensity.

To begin, the role of SPPs should be discussed. A thin metal slab with a negative refractive index over a broad frequency band is considered as a superlens and has been demonstrated to achieve a super resolution in the field of optical imaging.[27] When combined with a dielectric slab, e.g., Si, the collective displacement of electrons, which is often referred to as SPPs, can be generated at the interface between the superlens and the Si slab. Therefore, the sub-wavelength information is enhanced and can be recorded into the metallic "photoresist" to produce diffraction-unlimited patterns as the fabricated ultrathin PtNWs.[28] Thus, the concept of the superlens has applications in nanofabrication. Although the field of SPPs may decay exponentially with the increasing distance from the interface and has a small penetrating depth in metal and Si, it is mainly concentrated near the interface. Thus, the energy is remarkably enhanced in the near-field. Because of the impingement of the high energy,[29] a strong nonlinear optical response can be achieved at the interface; therefore, deep Si etching can be performed by applying direct LIL with a single nanosecond laser pulse.

To study the energy enhancement between the interface, finite-difference time-domain (FDTD) simulations (these methods are presented in our previous work[30]) were performed. Figures 2(a) and 2(c) show that the electric field was obviously enhanced when an 80-nm-thick Pt superlens was applied. The wave vector of the SPPs excited at the metal/dielectric interface is defined by the following equation:[31]

$$k_{\mathrm{p}} = k_{\mathrm{i}}\left(\frac{\varepsilon_{\mathrm{m}}\varepsilon_{\mathrm{d}}}{\varepsilon_{\mathrm{m}}+\varepsilon_{\mathrm{d}}}\right)^{1/2}, \quad (1)$$

where k_{p} and k_{i} represent the wave vectors of the SPPs and incident light, respectively. $\varepsilon_{\mathrm{m}}(\omega)$ is the permittivity of the metal, and $\varepsilon_{\mathrm{d}}(\omega)$ is the permittivity of the dielectric material. Both are frequency-dependent dielectric constants. The permittivity of Si, which is denoted as $\varepsilon_{\mathrm{d}}(\omega)$, is obtained from the Palik model, and $\varepsilon_{\mathrm{m}}(\omega)$ is obtained from the Lorentz–Drude oscillator model:[32]

$$\varepsilon_{\mathrm{m}}(\omega) = 1 - \frac{\omega_{\mathrm{p}}^2}{\omega^2 + i\Gamma_{\mathrm{p}}\omega} + \sum_{j=1}^{k}\frac{f_j\omega_j^2}{\omega_j^2 - \omega^2 - i\Gamma_j\omega}, \quad (2)$$

where ω_{p} is the plasma frequency, and Γ_{p} is the damping constant. k is the number of oscillators, whose frequency, strength, and damping constant are ω_j, f_j, and Γ_j, respectively.

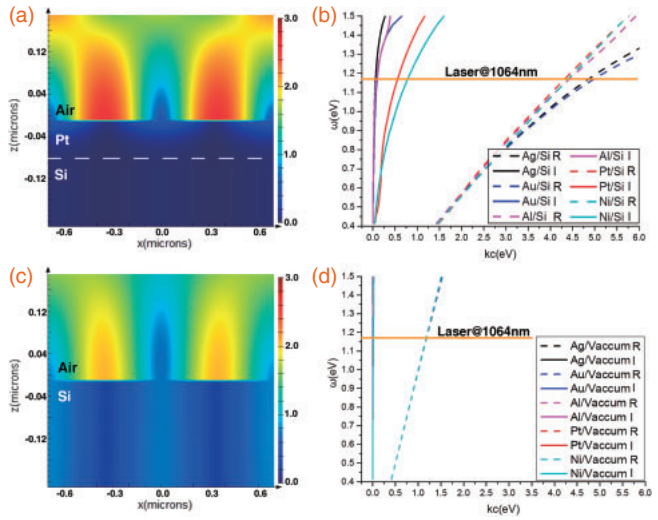

Fig. 2. Simulation of the electric-field distribution of the two-beam LIL pattern of a plane wave (a) with an 80-nm-thick Pt superlens and (c) without a superlens. Simulated SPP dispersion curves for (b) metal–Si and (d) metal–vacuum interfaces. The dashed and solid lines represent the real and imaginary parts, respectively.

The SPP dispersion law for the metal–Si [Fig. 2(b)] and metal–vacuum [Fig. 2(d)] interfaces indicates that the superlens can significantly enhance the energy around the interface when coupled with a Si substrate. The generated energy of the SPPs can reach 5 eV at a wavelength of 1,064 nm (1.17 eV). Therefore, when the wavelength of the impinging laser is 1,064 nm, the generated SPPs behave similarly to an ultraviolet ray, which can have a wavelength as short as 260 nm. Moreover, the evanescent waves are enhanced, and a super resolution can be achieved. To achieve a super resolution and obtain a specific ideal phenomenon, both the energy of the laser and the thickness of the superlens slab should be considered according to the simulation results (both the electric-field distribution shown in Fig. 2 and the absorption shown in Fig. 4).

As discussed above, the existence of the superlens dominates the smallest feature size of the fabricated metallic nanopatterns; however, the periodic and variable-sized characteristics of the patterns are due to the laser interference field distribution. Additional details are presented in our previous report.[25] Different kinds of nanopatterns are induced by the laser interference distribution, and the evolution pathway of the patterns is explained by the dewetting process of the metal film.

Compared with other near-field lithography technologies[33] that use metallic structures, for SELIL, the metallic superlens

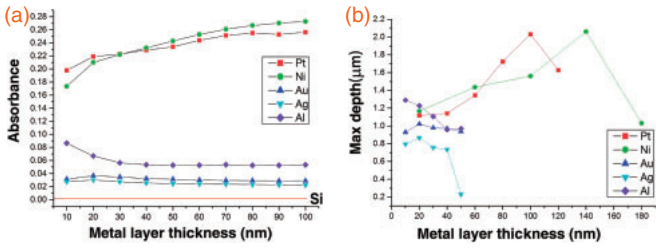

Fig. 4. (a) FDTD simulations of the absorption of five different superlens/Si systems with respect to the metal-layer thickness. (b) Maximum depths of the Si gratings after laser exposure, which agree well with the curves shown in (a).

is directly written to obtain sub-wavelength patterns owing to its high threshold. Thus, the mechanism of the interaction between the metallic film and the high-power laser pulse can be explained by the dewetting process.[34–37] The evolutionary pathway driven by the increase in the laser intensity of the Pt film on a Si substrate is shown in Fig. 3. Periodic Pt nanonetworks (PtNNs) are first formed after re-solidification at a low laser intensity. The distribution and diameters of the PtNNs are sensitive to the enhanced near-field energy change. More detailed structures of the PtNNs are shown in Fig. S2 in the online supplementary data at http://stacks.iop.org/APEX/11/000000/mmedia. Furthermore, ultrathin PtNWs are observed. Because the threshold of the metal is higher than that of the photoresist, by improving the threshold sensitization to the laser intensity and carefully controlling the energy, PtNWs with sub-wavelength features as small as several nanometers can be achieved. PtNWs with sub-50-nm feature sizes are shown in Fig. S3 in the online supplementary data at http://stacks.iop.org/APEX/11/000000/mmedia. For the higher laser intensity, the interconnected PtNNs and PtNWs are broken into nanodroplets via Rayleigh instability, and periodic Pt nanoparticles (PtNPs) with various sizes formed by Ostwald ripening[38] are observed, which results in the mass redistribution of the nanodroplets. Sub-10-nm PtNPs are clearly observed in Fig. S4 in the online supplementary data at http://stacks.iop.org/APEX/11/000000/mmedia. When the impinging energy is sufficiently high to obtain an evaporated metallic film, the strong nonlinear absorption of the metallic film results in an intense heat transfer to the Si substrate, and deep Si gratings are exposed. With the increase of the laser intensity, the exposed Si gratings melt, and ultimately, Si lattices are observed, which may be induced by the anisotropic ablation energy due to the different crystal orientation in monocrystalline Si. The thickness ranges of the applied Pt

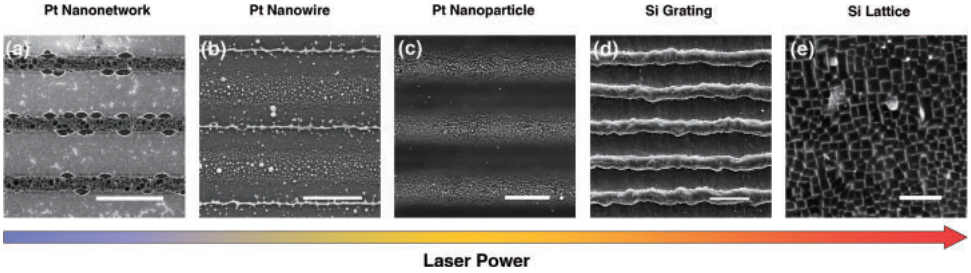

Fig. 3. Different energy thresholds result in distinct LIL patterns. The evolution of (a) PtNNs, (b) PtNWs, (c) PtNPs, (d) Si gratings, and (e) Si lattices, which greatly depends on the impinging energy. The scale bars in (a)–(e) represent 10, 2, 2, 10, and 1 μm, respectively.

superlens for forming different dewetting phenomena are detailed in the online supplementary data at http://stacks.iop.org/APEX/11/000000/mmedia.

The various diffraction-unlimited patterns (see Fig. 3) fabricated via SELIL are applicable in fields such as metamaterial manufacturing. For instance, PtNNs are useful in photochemical catalysis. Periodic variable-sized PtNPs are beneficial for plasmonic enhancement applications, e.g., in solar cells and surface-enhanced Raman scattering detection. The ultrathin PtNWs are potentially useful in electron-device fabrication, and the deep Si gratings exposed by SELIL can function as a mask for nanoimprinting.

Furthermore, we studied the direct-writing performance of the Si substrate by applying SELIL. As previously reported,[39] during the direct-writing process, the intense energy of the interference field was absorbed, and the Si surface was heated to its melting point. Thus, the absorbance of Si was a key factor affecting its direct-writing performance, and we simulated the absorbances of different kinds of superlens/Si systems via the FDTD method, as shown in Fig. 4(a). Here, the absorbance represents the total absorbance of the metallic film and the Si surface. To demonstrate the reliability of our simulation method, we simulated the absorbance of the Al film with the increase of the thickness, and the results agreed well with those reported by Aboelfotoh.[40] Details are presented in Fig. S5 in the online supplementary data at http://stacks.iop.org/APEX/11/000000/mmedia. We assumed that the absorbance and etching depth of the exposed Si gratings might be closely related; thus, we used a confocal microscope (Zeiss Axio CSM700) to measure the largest depth for different superlens/Si systems, as shown by Fig. 4(b). Figure S6 in the online supplementary data at http://stacks.iop.org/APEX/11/000000/mmedia shows detailed information about how we acquired the data. Notably, the etching depth curves and absorbance curves agree well with each other, and the maximum depth was >2 μm when a 100-nm-thick Pt superlens was applied, as shown in Fig. 4(b). Therefore, we hypothesize that the absorbance of the metallic film for vaporization is negligible at a reasonable thickness and that the energy absorbed by the system is mainly diffused to the Si substrate. However, when the metallic film is thick enough, the etching depth of Si eventually decreases because more energy contributes to the destruction of the metal layer.

Additionally, we performed control experiments. Bare Si samples without metal-layer coatings were prepared for SELIL. The samples were exposed to 150 pulses to achieve the same etching depths as the 100-nm Pt/Si system with a single pulse, as shown in Fig. 5. A large-scale area of Si gratings with a radius of approximately 100 μm is shown in Fig. 5(a). The surface shown in Fig. 5(b) is rough compared with that in Fig. 5(c), and the sectional views indicate that the grating period varies more regularly in Fig. 5(d) than in Fig. 5(e). It is likely that because of the high quenching rates of the metallic films, the rapid thermal annealing of the Si surface aided the release of the thermal strains, resulting in the smooth and fine profile of the gratings.

There is slight non-uniformity along the grating. This is caused by the re-solidification of molten Si, which results from the laser-induced explosive boiling[24] of the bumps during the direct-writing process of Si. However, such non-uniformity can be alleviated by improving the beam quality[41] and the processing method. Moreover, the non-uniform structures can be applied in many areas, such as the power and optical fields. For example, in our previous study, the Si surfaces were directly modified by multi-pulse laser interference to generate periodic hexagonally distributed hole structures,[21] which have superior anti-reflection and self-cleaning capabilities and are suitable for solar-cell applications. Compared with that shown in Fig. 5(c), the surface of the structure was rough [similar to that shown in Fig. 5(b)] because it was directly ablated by hundreds of laser pulses. In the present study, the superlens-enhanced explosive boiling effect preserved the smooth surface. Only a single pulse is needed; thus, the influence of unstable laser sources can be avoided.

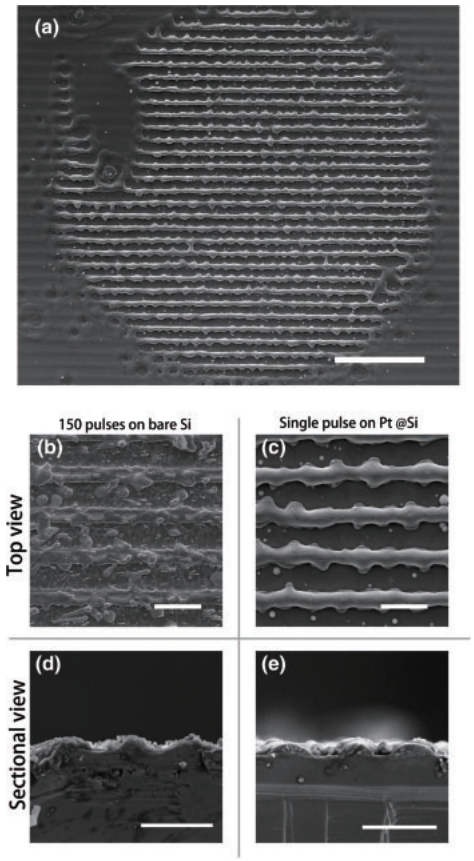

Fig. 5. (a) Large-scale area of exposed Si gratings under a single pulse. (b) Top view and (d) sectional view of bare Si samples exposed to 150 pulses. (c) Top view and (e) sectional view of a Si sample coated with a Pt superlens slab with a single laser pulse. The etching depths of the Si gratings of the two samples are approximately the same (2 μm). All the scale bars represent 10 μm, except for that in (a), which represents 50 μm.

In conclusion, SELIL is promising for sub-100-nm feature-size fabrication. Various sub-wavelength patterns, such as PtNNs, PtNWs, and PtNPs, were manufactured by applying a low-cost nanosecond laser source at a wavelength of 1,064 nm. These patterns are useful for applications in areas such as metamaterials. The direct-writing performance of Si with the aid of the superlens is ideal because the etching depth of the Si grating can reach 2 μm, and the surface profile is good.

Acknowledgments This work was supported by the National Key R&D Program of China (No. 2016YFE0112100), the EU H2020 Program (FabSurfWAR No. 644971; NanoStencil No. 767285), the National Natural Science Foundation Program of China (Nos. 11504030 and 61604018), the Jilin Provincial Science and Technology Program (Nos. 20160101318JC, 20160623002TC, 20180414002GH, 20180414081GH, and 20180520203JH), and the "111" Project of China (D17017).

1) K. Xu, D. Chen, F. Yang, Z. Wang, L. Yin, F. Wang, R. Cheng, K. Liu, J. Xiong, and Q. Liu, Nano Lett. **17**, 1065 (2017).
2) Y. Chen, Microelectron. Eng. **135**, 57 (2015).
3) X. Shi, P. Prewett, E. Huq, D. M. Bagnall, A. P. G. Robinson, and S. A. Boden, Microelectron. Eng. **155**, 74 (2016).
4) Q. He, C. Tan, and H. Zhang, ACS Nano **11**, 4381 (2017).
5) Z. Gan, Y. Cao, R. A. Evans, and M. Gu, Nat. Commun. **4**, 2061 (2013).
6) N. Kooy, K. Mohamed, L. T. Pin, and O. S. Guan, Nanoscale Res. Lett. **9**, 320 (2014).
7) D. Ji, T. Li, and H. Fuchs, Adv. Electron. Mater. **3**, 1600348 (2017).
8) K. Du, J. Ding, I. Wathuthanthri, and C. H. Choi, Nanotechnology **28**, 465303 (2017).
9) F. Q. Zhang, K. Q. Peng, R. N. Sun, Y. Hu, and S. T. Lee, Nanotechnology **26**, 375401 (2015).
10) D. Xia, Z. Ku, S. C. Lee, and S. R. Brueck, Adv. Mater. **23**, 147 (2011).
11) T. H. Lin, Y. K. Yang, and C. C. Fu, Nanotechnology **28**, 475301 (2017).
12) C.-H. Chang, Y. Zhao, R. K. Heilmann, and M. L. Schattenburg, Opt. Lett. **33**, 1572 (2008).
13) L. Müller-Meskamp, Y. H. Kim, T. Roch, S. Hofmann, R. Scholz, S. Eckardt, K. Leo, and A. F. Lasagni, Adv. Mater. **24**, 906 (2012).
14) D. A. Bacon-Brown and P. V. Braun, Adv. Opt. Mater. **6**, 1701049 (2018).
15) H. Ning, J. H. Pikul, R. Zhang, X. Li, S. Xu, J. Wang, J. A. Rogers, W. P. King, and P. V. Braun, Proc. Natl. Acad. Sci. U.S.A. **112**, 6573 (2015).
16) J. H. Seo, J. H. Park, S. I. Kim, B. J. Park, Z. Ma, J. Choi, and B. K. Ju, J. Nanosci. Nanotechnol. **14**, 1521 (2014).
17) L. Wang, L. Dong, L. Li, Z. Weng, H. Xu, M. Yu, and Z. Wang, J. Mater. Sci. **53**, 3239 (2018).
18) X. Zhang and Z. W. Liu, Nat. Mater. **7**, 435 (2008).
19) E. D. Palik, *Handbook of Optical Constants of Solids I* (Academic Press, San Diego, CA, 1985) Vol Subpart 2.
20) V. Zorba, N. Boukos, I. Zergioti, and C. Fotakis, Appl. Opt. **47**, 1846 (2008).
21) T.-H. Chen, R. Fardel, and C. B. Arnold, Light: Sci. Appl. **7**, 17181 (2018).
22) L. Zhao, Z. Wang, J. Zhang, L. Cao, L. Li, Y. Yue, and D. Li, Appl. Surf. Sci. **346**, 574 (2015).
23) T. Tavera, N. Pérez, A. Rodríguez, P. Yurrita, S. M. Olaizola, and E. Castaño, Appl. Surf. Sci. **258**, 1175 (2011).
24) V. Craciun, N. Bassim, and R. K. Singh, Appl. Surf. Sci. **186**, 288 (2002).
25) J. Xu, Z. Wang, Z. Zhang, D. Wang, and Z. Weng, J. Appl. Phys. **115**, 203101 (2014).
26) F. L. Gonzalez, D. E. Morse, and M. J. Gordon, Opt. Lett. **39**, 13 (2014).
27) N. Fang, H. Lee, C. Sun, and X. Zhang, Science **308**, 534 (2005).
28) L. Li, Z. Wang, W. Li, K. Peng, Z. Zhang, M. Yu, Z. Song, Z. Weng, D. Wang, and L. Zhao, Appl. Phys. Lett. **107**, 133104 (2015).
29) A. Krasnok, M. Tymchenko, and A. Alù, Mater. Today **21**, 8 (2018).
30) L. Li, K.-Q. Peng, B. Hu, X. Wang, Y. Hu, X.-L. Wu, and S.-T. Lee, Appl. Phys. Lett. **100**, 223902 (2012).
31) I. I. Smolyaninov, Y. J. Hung, and C. C. Davis, Science **315**, 1699 (2007).
32) B. H. Cheng, Y. C. Lan, and D. P. Tsai, Opt. Express **21**, 14898 (2013).
33) Z. Liu, A. Qihuo Wei, and X. Zhang, Nano Lett. **5**, 957 (2005).
34) J. Bischof, D. Scherer, S. Herminghaus, and P. Leiderer, Phys. Rev. Lett. **77**, 1536 (1996).
35) H. Krishna, R. Sachan, J. Strader, C. Favazza, M. Khenner, and R. Kalyanaraman, Nanotechnology **21**, 155601 (2010).
36) A. Sharma and R. Khanna, Phys. Rev. Lett. **81**, 3463 (1998).
37) S. Strobel, C. Kirkendall, J. B. Chang, and K. K. Berggren, Nanotechnology **21**, 505301 (2010).
38) Z. Zhou, Z. Song, L. Li, J. Zhang, and Z. Wang, Appl. Surf. Sci. **335**, 65 (2015).
39) C. Y. Chao, C. Y. Chen, C. W. Liu, Y. Chang, and C. C. Yang, Appl. Phys. Lett. **71**, 2442 (1997).
40) M. O. AboelFotoh and R. J. von Gutfeld, J. Appl. Phys. **43**, 3789 (1972).
41) C. Chen, P. Konkola, R. Heilmann, C. Joo, and M. Schattenburg, Proc. SPIE **4936**, 126 (2002).

